RSC Advances

PAPER

View Article Online
View Journal | View Issue

Cite this: *RSC Adv.*, 2025, **15**, 47066

Harnessing anisotropy in liquid crystal elastomer based lithium-ion gel-polymer batteries

Zakaria Siddiquee, [a] Weinan Xu[b] and Antal Jákli *[c]

Received 3rd October 2025
Accepted 17th November 2025

DOI: 10.1039/d5ra07527k

rsc.li/rsc-advances

Recently we showed the potential of unaligned lithium-ion doped nematic Liquid Crystal Elastomer (LCE)-based quasi-solid (gel-polymer) electrolytes for batteries demonstrating excellent charge–discharge capacities. In this work, we study the effect of the alignment of LCE on the battery performance. We report the first investigation of homeotropically aligned LCEs in lithium-ion batteries and systematically compare their performance with planar aligned samples. We demonstrate that with increased ionic liquid (IL) loading, the homeotropic alignment (director is perpendicular to the electrodes) exhibits higher conductivity compared to planar alignment (director is parallel to the electrodes), underscoring the tunability of LCE-based electrolytes. The samples with the highest IL loading in both alignments exhibit a room temperature conductivity of ~1 mS cm^{-1} and an electrochemical stability window of ~4.8 V. Additionally we find that LCE based batteries with homeotropic alignment charge more rapidly. These findings provide new insights into optimizing electrolyte performance through liquid crystal alignment control, thereby advancing the development of lithium-ion batteries.

1. Introduction

Lithium-ion batteries (LIBs) are the backbone of modern portable electronics, electric vehicles (EVs), and renewable energy storage systems, prized for their high specific energy and long cycle life.[1,2] However, safety concerns continue to hinder their full potential. These issues largely stem from the flammable, volatile organic solvents in conventional liquid electrolytes, which are prone to thermal runaway, leakage, and the formation of lithium dendrites that can lead to catastrophic failure.[3–6] To address these safety limitations, solid-state electrolytes (SSEs) have been proposed as an alternative, offering improved thermal stability and mechanical robustness.[7–10] Among them, solid polymer electrolytes (SPEs) are particularly attractive for their processability, flexibility, and compatibility with various electrodes. Despite this promise, traditional SPEs, especially those based on poly(ethylene oxide) (PEO), suffer from low ionic conductivity at room temperature and poor interfacial stability,[11–18] and it remains challenging to simultaneously achieve high conductivity and mechanical durability.[14,17,19–21]

A promising direction to overcome these limitations involves the integration of liquid crystal (LC) materials into polymer systems. LCs exhibit a unique combination of anisotropic molecular ordering and fluidity, which allows for the self-assembly of ion-conducting pathways.[22–24] The anisotropy inherent to LC phases can be harnessed to facilitate directional ion transport and potentially suppress dendrite formation through improved ion distribution.[25–27] Building on this, liquid crystal elastomers (LCEs) merge the anisotropic molecular ordering of liquid crystals with the elasticity and toughness of crosslinked polymer networks.[28,29] This unique duality enables LCEs to form self-supporting membranes that combine ion-conductive structure, mechanical robustness, and tunability under external stimuli.[30,31] Recent studies have confirmed that LCEs can serve as viable hosts for lithium salts and ionic liquids, forming gel-polymer electrolytes with enhanced conductivity and thermal stability.[32,33] The mechanism for this is rooted in their molecular design; common LC monomers such as RM257 possess an ether-rich backbone that promotes Li^+ transport, while their ability to form aligned mesophases provides mechanical integrity upon polymerization.[34,35] These ordered nanostructures can serve as effective ion-conduction channels, and the orientational elasticity of the LCE network may also play a crucial role in suppressing lithium dendrite formation. While prior works have assessed the effect of molecular alignment in fluid LC phases, the influence of long-range macroscopic alignment locked into the polymer network of an elastomer has not been reported on battery performance.

In this work, we present the first demonstration of homeotropically aligned LCEs (director perpendicular to the electrodes), systematically compared with planar alignment (director parallel) in lithium-ion batteries. By maintaining

[a]*Department of Physics, Kent State University, Kent, OH, 44242, USA*
[b]*School of Polymer Science and Polymer Engineering, University of Akron, Akron, Ohio, 44325, USA*
[c]*Materials Science Graduate Program and Advanced Materials and Liquid Crystal Institute, Kent, OH, 44242, USA. E-mail: ajakli@kent.edu*

a fixed polymer backbone and crosslinking chemistry while varying the alignment of LC domains and the concentration of ionic liquid, we elucidate the specific role of mesophase orientation on Li-ion transport properties. We evaluate how this molecular orientation impacts ionic conductivity, lithium transference number, and interfacial resistance. Our findings clearly show that macroscopic alignment is a critical parameter for tuning electrochemical performance.

2. Materials and sample preparations

2.1. Materials

The gel-polymer electrolytes developed in this study leverage the unique anisotropic structure and stimuli-responsive nature of ionic liquid infused liquid crystal elastomers, positioning them as promising candidates for lithium-ion battery applications. The bifunctional liquid crystal monomer 1,4-bis[4-(3-acryloyloxypropyloxy)benzoyloxy]-2-methylbenzene (RM257, 97%, (see Fig. 1)) was obtained from SYNTHON-Chemicals (Germany) and used as the primary LC mesogen in the formulation of the LCE matrix. It contains ether oxygen groups that naturally facilitate the formation of two-dimensional ion-conducting nanochannels. These channels enable efficient lithium-ion transport by reducing migration barriers. The rigid benzene rings present in RM257 further strengthen the polymer network, contributing to its mechanical robustness.

Elastomers made solely from liquid crystal monomers are often too brittle for practical use. To address this, a small amount of thiol-functionalized chain extender 2,2-(ethylenedioxy)diethanethiol (EDDET, 95%) was introduced to improve flexibility by elongating the polymer chains[36]—an approach well-documented in prior research.[32,37]

The ionic liquid 1-butyl-3-methylimidazolium bis(trifluoromethylsulfonyl)imide (BMIM-TFSI, 97%) was used to enhance ionic conductivity by providing a mobile ion transport medium within the polymer network (see Fig. 1 for the molecular structure).

Pentaerythritol tetrakis-(3-mercaptopropionate) (PETMP, 95%) was used as the tetrafunctional thiol crosslinker to construct a three-dimensional network. The Michael addition reaction was catalyzed by dipropylamine (DPA, 99%), while 2,6-di-*tert*-butyl-4-methylphenol (BHT, 99%) was added as a thermal inhibitor to prevent premature crosslinking. Lithium bis-trifluoromethanesulfonimidate (LiTFSI, 98%), salt was used as the lithium-ion source due to its high electrochemical stability and compatibility with both the ionic liquid and the LCE matrix.

Photopolymerization was initiated using 2,2-dimethoxy-2-phenylacetophenone (Irgacure-651, 99%) under UV exposure. Except for RM257, all chemical reagents were purchased from Sigma-Aldrich (Milwaukee, USA) and used without further purification unless otherwise stated.

Lithium metal disks (~600 μm thickness) and lithium iron phosphate ($LiFePO_4$) cathode materials were sourced from MSE Supplies (Tucson, Arizona, USA) and used for battery fabrication and electrochemical testing.

2.2. Fabrication and alignment of LCE electrolytes

For c < 20 wt% IL concentrations the RM257-based elastomer retains a stable nematic phase between 50 and 100 °C, enabling

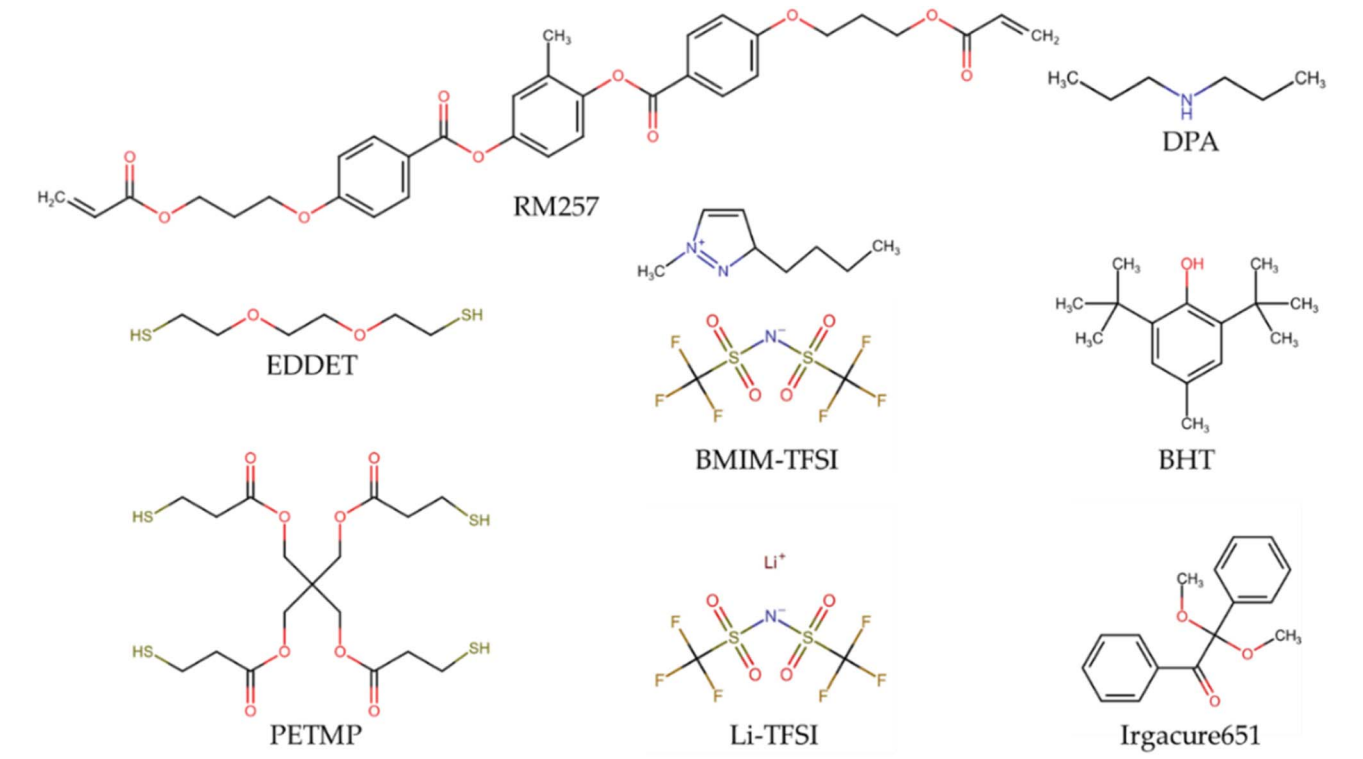

Fig. 1 Chemical structures of the materials used for liquid crystal elastomer-based gel-polymer electrolytes.

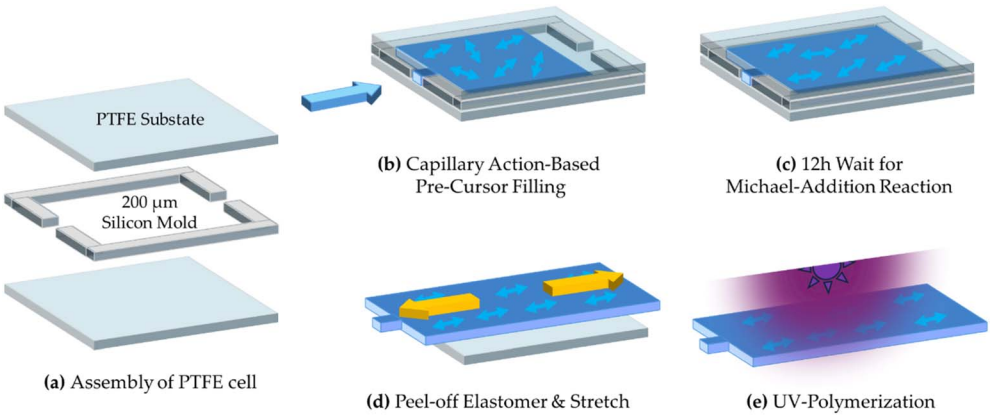

Fig. 2 Schematic illustration of the fabrication process for planar-aligned liquid crystal elastomer electrolytes (LCE-P*n*). (a) Illustration of polytetrafluoroethylene (PTFE) sandwich cell mold used for precursor injection and alignment; (b–e) steps of the alignment and curing process. Alignment direction shown by yellow arrows.

a simple alignment process through thermal annealing between rubbed polyimide-coated substrates. In contrast, high IL concentrations destabilize the nematic phase—particularly in the absence of thiol-based chain extenders—shifting the isotropic–nematic transition temperature below room temperature. This shift inhibits effective alignment through surface treatment alone, necessitating a two-stage polymerization strategy adapted from Saed *et al.*,[37] with modifications according to Zhang *et al.*[38]

To prepare the precursor mixture, 500 mg of RM257 was dissolved in 40 wt% toluene along with 1.33 mg of BHT and 3.77 mg of Irgacure-651. The mixture was heated to 80 °C and then cooled to room temperature to acquire a solution. Upon cooling, 105.7 mg of EDDET and 47.1 mg of PETMP were added and homogenized using ultrasonic dispersion. The thiol group content was selected based on the work by Wang *et al.*, where they achieved optimal ionic conductivity while preserving structural stability.[32]

We fabricated samples in both planar (P) and homeotropic (H) configurations across five different IL concentrations. The samples are denoted as LCE-X*n*, where X indicates the alignment (P = planar, H = homeotropic) and the suffix *n* in increasing order from 1 to 5 correspond to 0.67, 23, 40, 57.1 and 66.7 wt% IL concentrations, respectively. For full composition details see Table S1.

To form the precursor, the polymer-monomer solution and the prepared IL-component solution were rapidly combined and vortex-mixed for 5 minutes. To prevent crystallization of RM257, the solution was gradually reheated to 80 °C and then cooled to room temperature. For samples LCE-X1 through LCE-X4, 78.4 mg of (2 wt% in toluene) DPA solution was used as catalyst. For sample LCE-X5, a lower 78.5 mg of (0.5 wt% in toluene) DPA solution was used. This was necessary because the higher ionic-liquid concentration (2 wt%) was found to accelerate the reaction, leading to an undesirable isotropic phase in later post-stretching steps. A comparison of LCE-X5 samples prepared with 0.5 wt% and 2 wt% DPA is available in Fig. S8. These mixtures were vortexed until they transitioned from a low-viscosity, water-like fluid to a moderately viscous state exhibiting increased flow resistance. This change suggests the onset of weak viscoelastic behavior, though the mixture remained homogeneous and pourable. The precursor formulation was prepared through a two-stage thiol–acrylate Michael addition reaction.

For planar alignment, a sandwich cell type mold was fabricated by assembling 200 μm-thick silicone sheets sourced from Generic (Peoples Republic of China) with 254 μm-thick Polytetrafluoroethylene (PTFE) sheets sourced from ePlastics (San Diego, USA). The PTFE sheets were cut and affixed to one side of glass substrates using Norland 65 UV-curable adhesive. The silicone mold was then shaped as shown in Fig. 2 and sandwiched between the PTFE-coated glass substrates with the PTFE surfaces facing the silicone spacer. The assembled mold was pressed and baked in a 25.4 torr vacuum oven at 100 °C for 1 hour to ensure a robust and sealed alignment cell. The mold was filled with the LCE precursor solution and left undisturbed for 24 hours to allow the Michael addition reaction to proceed. After initial network formation, the film was peeled from the mold, mechanically stretched to induce uniform planar alignment along the stretching, and subsequently UV-cured under 65 mW cm^{-2} UV light (320–390 nm) for 30 seconds to lock in the orientation and form the final elastomer electrolyte.

Homeotropic alignment was achieved using a cylindrical PTFE mold, by covering the inner surface of glass capillaries from Cole-Parmer (Vernon Hills, USA) with PTFE sheets. The PTFE was cut to size and adhered to the inner surface of the capillaries using Norland 65 adhesive. Once the Michael addition reaction initiated and the precursor began to set, the material was injected into the alignment cells *via* capillary action. The flow induced by filling promoted director alignment parallel to the flow, which was preserved as the network formation progressed. The filled cells were maintained at room temperature for 8 hours in darkness to allow completion of the initial stage of crosslinking, followed by demolding. The resulting LCE samples aligned along the axis of the cylinder were then mechanically stretched to 150% along the alignment axis and UV-cured at 65 mW cm^{-2} intensity to lock in the alignment using an IntelliRay 600 UV flood curing system with

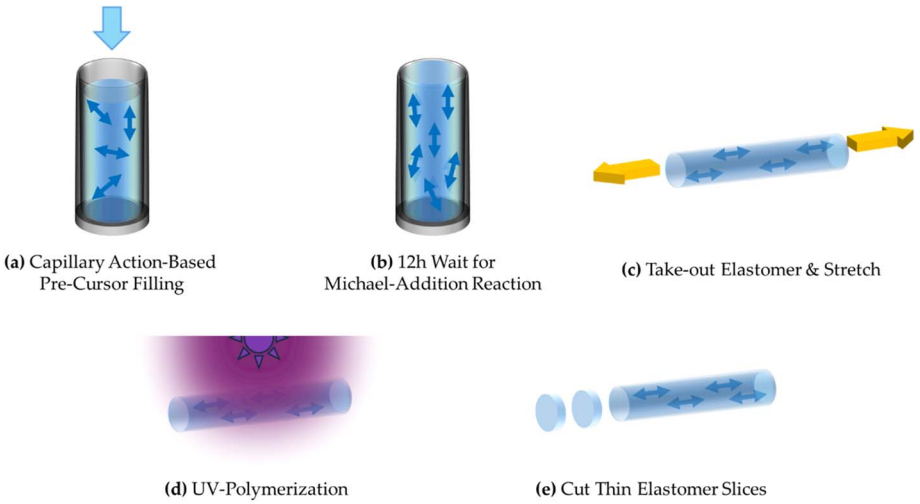

Fig. 3 Schematic illustration of the fabrication process for homeotropically aligned LCE electrolytes (LCE-H*n*). (a–e) Steps of the alignment and curing process. Alignment direction shown by yellow arrows.

an operating UV range from 320–390 nm. The polymerization is completed rapidly between 15 and 30 seconds due to efficient thiol-((meth)acrylate) and ene–ene crosslinking, with all reactive groups consumed after the exposure period.[39] FTIR analysis supports this observation, showing the disappearance of the characteristic S–H stretching peak at 2507 cm^{-1}—attributed to RM257, EDDET, and PETMP—and the appearance of a C=C stretching peak at 1606 cm^{-1}, confirming complete conversion (see Fig. S1(a) for pre-cursor materials and Fig. S1(b and c) for macroscopically aligned electrolytes).[37,40]

The cylindrical samples were then sectioned into 100 μm-thick discs with director alignment normal to the plates of the discs using a microtome to yield the final homeotropically aligned elastomer films as shown in Fig. 3.

3. Results and discussion

3.1. Nanostructure and macroscopic alignment

The 1D and 2D Wide-Angle X-ray Scattering (WAXS) patterns are shown in Fig. S2 and S3, respectively. These measurements were performed on planar (LCE-P*n*) and homeotropic (LCE-H*n*) liquid crystal elastomer electrolytes using a 5 minute exposure time. LCE-P1 has two lobes left and right the direct beam indicating director alignment in the vertical direction. The azimuthal distribution of the WAXS peaks increase upon increasing n values (*i.e.*, with increasing IL concentration) indicating decreasing alignment. The degree of the alignment S can be quantified by the Hermans–Stein orientation distribution function,[41,42] $S = \frac{3\langle\cos^2\phi\rangle - 1}{2}$ where ϕ is the azimuthal angle between the director and the alignment axis and $\langle\cos^2\phi\rangle$ is calculated from the azimuthal dependence of the scattered intensity $I(\phi)$ as $\langle\cos^2\phi\rangle = \frac{\int_0^{\frac{\pi}{2}} I(\phi)\sin\phi\cos^2\phi\,d\phi}{\int_0^{\frac{\pi}{2}} I(\phi)\sin\phi\,d\phi}$. Higher values of S (approaching 1) indicate perfect alignment, while lower values (near 0) reflect poorly aligned systems.[43–45] Analyzing the azimuthal distribution of the 2D patterns shown in Fig. 4(a) we get that LCE-P1 had the highest nematic order parameter: ~0.46 ± 0.02. The samples LCE-P2 to LCE-P4, as shown in Fig. S3(a–c), with intermediate ionic content have orientation order parameters between 0.28 to 0.33. In Fig. S3(d), LCE-P5 with the largest ionic content exhibited the lowest value: 0.16 ± 0.03, showing a systematic decrease of the orientational order parameter with increasing IL content. This shows that the IL disrupts molecular orientational order.

The 2D scattering pattern of LCE-H1 in Fig. 4(b) shows a ring pattern indicating director alignment along the X-ray beam. The peak positions at $q \approx 1.4$ $Å^{-1}$, for both planar and homeotropic

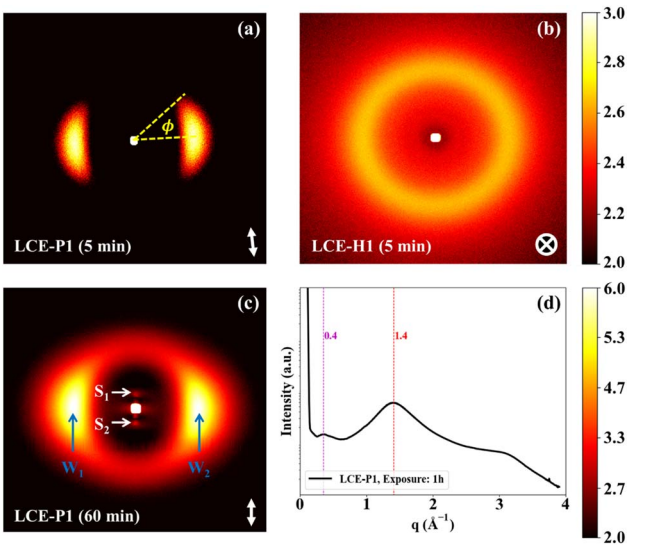

Fig. 4 Wide Angle X-ray (WAXS) analysis of LCE-X1 before use in batteries. White double-sided arrows indicate original alignment directions. Panels show 2D profiles of (a) LCE-P1 and (b) LCE-H1 at 5 min exposure. Panel (c) shows the 2D profile and (d) the corresponding 1D spectrum for LCE-P1 at 1 h exposure. White double-sided arrows and circle with a cross show the alignment direction in the plane and normal to it, respectively.

cells correspond to a lateral spacing between long axis of the mesogens of $d = 2\pi/Q \approx 4.5$ Å.

Long (1 hour) exposure of LCE-P1 also shows two minor peaks (S_1, S_2) oriented along the vertically oriented director at $Q \approx 0.4$ Å^{-1}, indicative of smectic clusters with layer spacings $d = 2\pi/q \approx 15.7$ Å. This is shown in Fig. 4(c) at 22.4 °C. This observation aligns with previous studies of nematogen polymers, which report that the introduction of flexible spacers into the polymer backbone promotes the formation of smectic phases.[46] In liquid crystal elastomers, longer flexible spacers such as thiol extensions allow mesogen to organize into layered structures more readily, stabilizing smectic domains. The q-dependence of the scattering intensity integrated over azimuthally is shown in Fig. 4(d).

After drying under vacuum at 100 °C for 24 hours, each sample was placed between crossed polarizers at four orientations—0°, 45°, 90°, and 135°—with 0° and 90° corresponding to the directions of the polarizer and analyzer, respectively. POM images were captured after the polymerization process as shown in Fig. S4–S8. POM textures of 100 μm thick LCE-Xn (n = 1–5) samples after polymerization are shown in Fig. 5 at 0°, 45° orientations between crossed polarizers (note 0° and 90°, furthermore, 45°and 135° give the same information). The LCE-Pn (n = 1–5) samples displayed extinction at 0° and 90°, with maximum brightness at 45°, confirming planar director alignment with decreasing quality with increasing IL content (see Fig. 5(a)) in agreement with the XRD observations shown in Fig. S3(a–d). In LCE-Hn (n = 1–5) cells the POM images are dark for all n both at 0° and 45°as seen in Fig. 5(b) and S3(e, f) verifying director alignment very close to perpendicular to the substrates. Note that the increasing darkness toward large IL content is due to the decreasing quality of the alignment providing quasi isotropic orientation distribution.

Field Emission-Scanning Electron Microscopy (FE-SEM) images of 100 μm thick planar and homeotropic samples without prior drying are shown in Fig. S9. The IL contents

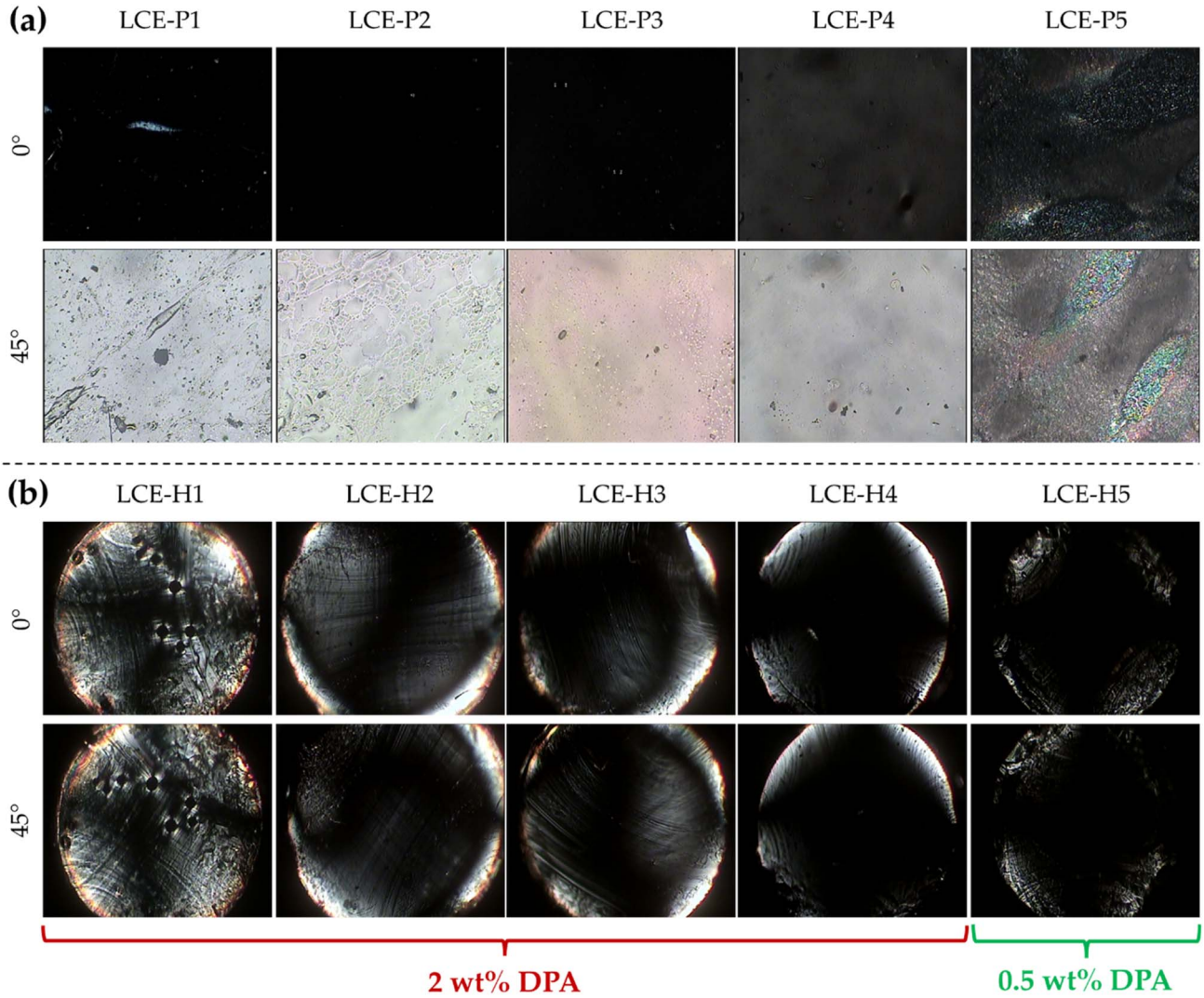

Fig. 5 POM textures of 100 μm thick LCE-Xn (n = 1, 2, 3, 4, 5) electrolytes observed under crossed polarizers at rotation angles of 0° and 45° with respect to the crossed polarizers for: (a) planar-aligned (LCE-Pn) and (b) homeotropically-aligned (LCE-Hn) samples. The DPA concentration used for each electrolyte's preparation is indicated below its respective POM images.

appear in form of pores and indicate a correlation between IL concentration and pore formation within the polymer matrix.

3.2. Ionic conductivity

The temperature dependence of ionic conductivity (σ) was investigated using electrochemical impedance spectroscopy (average of 3 measurements per specific electrolyte). The ionic conductivity was calculated using the equation: $\sigma = \frac{l}{A \cdot R_b}$, where l is the thickness of the electrolyte film, R_b is the bulk resistance obtained from the Nyquist plots shown in Fig. S10 and S11, and A is the contact area of the Stainless Steel electrodes.

In Fig. 6(a) the ionic conductivity in logarithmic scale is plotted against $1000/T$ (K^{-1}) for LCE-Xn (n = 1–5) with both planar and homeotropic alignments at different ionic liquid concentrations. For all samples the plots can be fitted by linear function, indicating Arrhenius behavior: $\sigma \propto \exp\left(\frac{-E_a}{k_B T}\right)$, where k_B is the. Boltzmann constant and E_a is the activation energy that can be obtained from the slope of the linear fit.

The averaged values of E_a are plotted in Fig. 6(b) as function of IL concentration for both the planar and homeotropic samples. For the pure and with c < 25% IL concentrations LCEs, both alignments have activation energies of 0.61 ± 0.01 eV. For c > 25%, LCE-Xn (n = 2–4) the homeotropic-aligned samples demonstrated lower activation energies suggesting more favorable ion conduction along the director. Just as for the conductivity values, for LCE-P5 and LCE-H5 samples the activation energies are again the same within the measurement error reflecting the bulk properties of the IL rather than structured transport through the polymer. Tables S2 and S3 list the average conductivity values at various temperatures for planar and homeotropic cells, respectively. By increasing IL concentrations, ionic conductivity improves markedly reaching σ > 1 mS cm^{-1} for LCE X5 samples. This demonstrates that the ion-conducting properties of the material can be tuned by simply modifying IL content while maintaining the same polymer backbone.

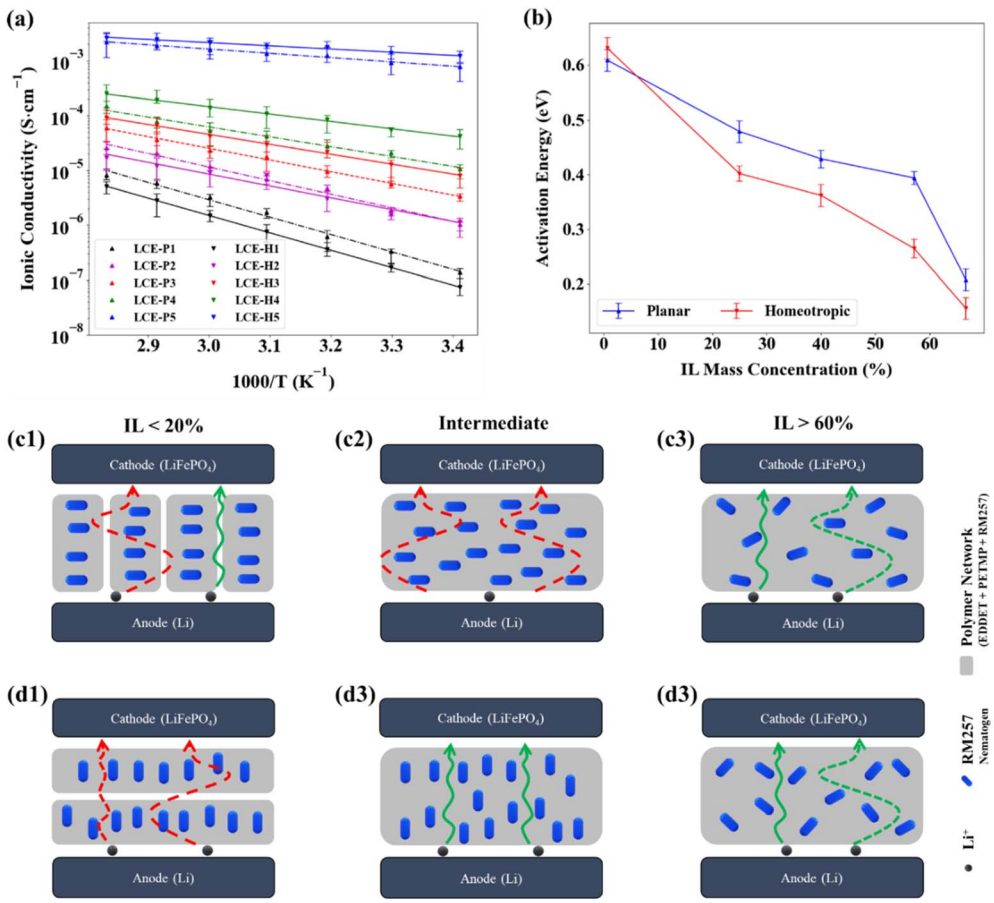

Fig. 6 Summary of the results of the ionic conductivity measurements. (a) Ionic conductivity in logarithmic scale as function of $1000/T$ (Arrhenius plot) of LCE electrolytes for planar (upright triangles fitted with dashed lines) and homeotropic (downward triangles fitted with solid lines) alignments. (b) The IL mass concentration dependence of the activation energies of the Arrhenius plots shown in (a). (c1–c3) and (d1–d3) Schematic of the proposed anisotropic Li^+ transport mechanism in planar and homeotropic LCE electrolytes. At low IL (<20%) concentration (c1 and d1), smectic-like domains create favorable 1D channels in the planar alignment. At intermediate IL concentration (c2 and d2), there are no smectic domains, and the ion conduction favors the homeotropic alignment. At high IL (>60%) concentration (c3 and d3), the swollen, isotropic network minimizes the alignment effect, resulting in similar conductivity for both configurations. The red and blue arrows depict slow and fast ion transport modes, respectively.

The interpretation of these results is depicted schematically in Fig. 6c(1–3) and d(1–3) for the planar and homeotropic cells, respectively and can be explained as follows.

At low IL concentrations (LCE-X1, LCE-X2), the higher ionic conductivity in the planar aligned samples can be attributed to smectic-like correlations, which were revealed as weak small-angle diffraction spots under long exposure for these low-IL samples, shown in Fig. 4(c and d). Where smectic layering occurs, ion diffusion is suppressed normal to the layers (along the director). As depicted in Fig. 6(c1), in planar alignment these transient smectic layers orient perpendicular to the electrodes creating more favorable, quasi-2D pathways for Li^+ transport between the electrodes. Conversely, in the homeotropic alignment, shown in Fig. 6(d1), these layers lie parallel to the electrodes, suppressing ion movement and forcing a more indirect path, thus resulting in lower conductivity of LCE-H1 than of LCE-P1.

At intermediate IL concentration the smectic clusters are suppressed by the IL and the ions move preferably along the director. This is due to the Lewis acid-base coordination in which the lithium ions migrate by coordinating with electron-rich ether groups in the polymer backbone, which act as Lewis bases and donate electron density to stabilize Li^+ cations.[47–50] This coordination promotes ion dissociation and hopping transport along the director. As shown schematically in Fig. 6(c2), in planar alignment the director lies parallel to the substrate, producing long lateral channels that enhance in-plane conduction. As shown in Fig. 6(d2), in homeotropic alignment the director is normal to the electrodes and the ion conduction between electrodes is enhanced.[51] This leads to more than a factor of 2 higher conductivity of the homeotropic cells at moderate IL concentrations (LCE-H3 and H4) as seen in Fig. 6(a).

At the highest IL concentration evaluated (LCE-X5), as depicted in Fig. 6(c3 and d3), the system becomes oversaturated and the LCE network swells significantly with free ionic liquid. This process disrupts much of the long-range nematic order, leading to quasi-isotropic behavior, and ion transport becomes dominated by diffusion through the bulk IL phase. As a result, the performance difference between the two configurations is minimized. This suggests that even in this highly swollen state, some small degree of alignment effect is retained, and the homeotropic orientation continues to offer a marginally more efficient pathway for ion transport. This leads to the only slightly higher conductivity of LCE-H5 than LCE-P5 as seen in Fig. 6(a).

3.3. Electrochemical properties

The lithium-ion transference number (t_{Li^+}), representing the fraction of ionic current carried by lithium ions, was determined using the Bruce–Vincent–Evans equation.[52] The required parameters were obtained using standard chronoamperometry, as shown in Fig. S12. A constant DC bias of 10 mV was applied for 10 000 seconds to record the initial current (I_0) and steady-state current (I_s).[53] The interfacial resistances before (R_0) and after (R_s) polarization were obtained from EIS (the resistance value represents the average of three separate EIS measurements, whereas the fall current was measured a single time for each sample).[52,53]

The test results for the Li/LCE-Xn/Li (n = 2–5) symmetric cells at room temperature are presented in Fig. S12(d). LCE-X1 was excluded from testing due to its low ionic conductivity at room temperature, which significantly impaired battery performance. The measured t_{Li^+} values range between 0.62 and 0.69, with the homeotropic alignment showing slightly higher transference numbers. A higher transference number contributes to improved performance by reducing concentration gradients during cycling, thereby minimizing the risk of dendrite formation and enhancing interfacial stability. These characteristics collectively support higher coulombic efficiency and longer cycle life, positioning aligned LCEs as promising candidates for next-generation lithium-ion batteries. The 0.69 transference number exhibited by LCE-X5, is promising for fast-charging applications. However, there are trade-offs. While IL improves ion mobility, it also reduces the mechanical strength of the polymer network and makes alignment more difficult. As a result, even though LCE-X5 was found to achieve the highest lithium-ion transference number among the series, the alignment effect is disappearing.

Symmetric Li/LCE-X4/Li cells were used to study the electrochemical stability of the LCE-X4 electrolyte and its interaction with metallic lithium. This test was performed on cells containing both planar and homeotropic electrolytes as shown in Fig. 7(a and b) where the excellent stability of the cell and electrodes are demonstrated. It shows a stable voltage response where the amplitudes ~0.026 V do not change significantly with time, even after 500 cycles, for both alignment cases using 0.1 mA cm^{-2} current density.

To investigate the redox behavior under operating conditions, Li/LCE-X4/$LiFePO_4$ and Li/LCE- X5/$LiFePO_4$ batteries were assembled and examined at 22.4 °C using cyclic voltammetry (CV). Redox peaks with symmetrical profiles were observed (single measurement per specific full cells) at approximately 4.2

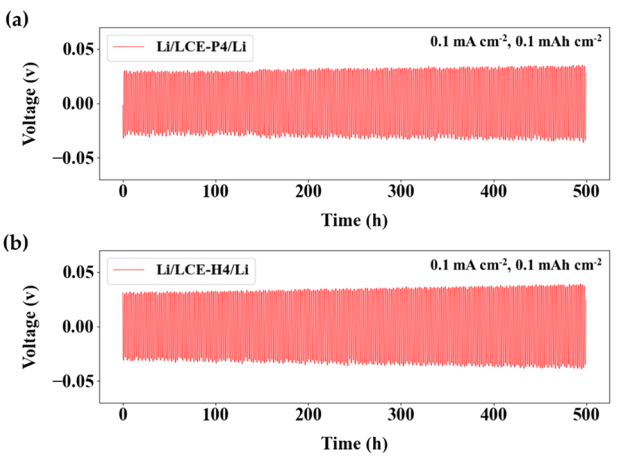

Fig. 7 Voltage profiles of symmetric Li/LCE-X4/Li cells at 0.1 mA cm^{-2} current density and 0.1 mAh cm^{-2} cycling capacity. (a) Planar alignment; (b) homeotropic alignment.

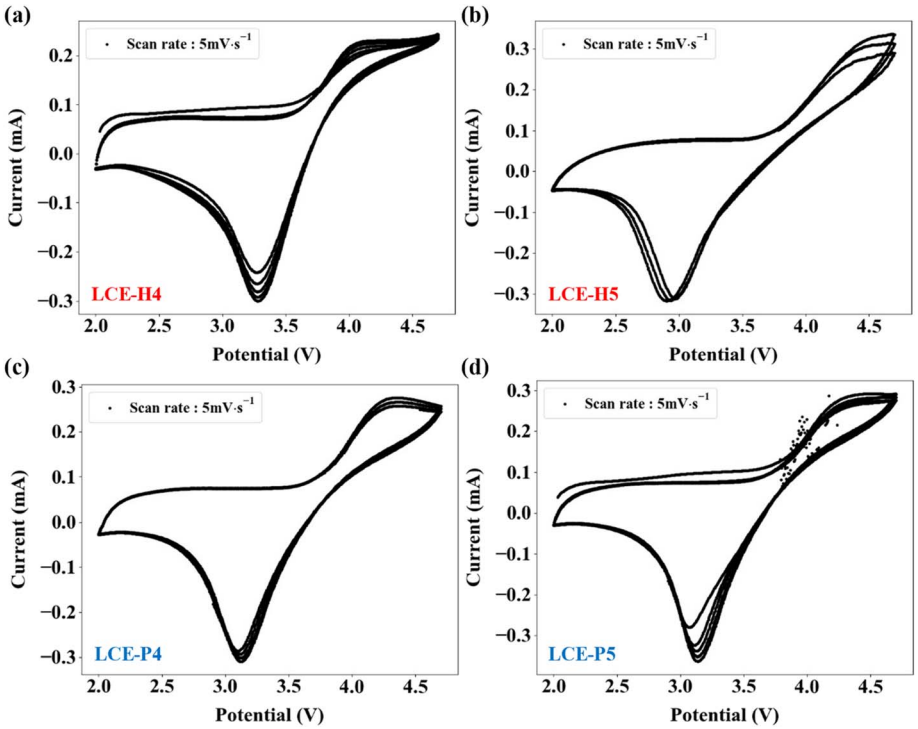

Fig. 8 Cyclic voltammograms recorded at 5 mV s^{-1} scan rate for (a) Li/LCE-H4/$LiFePO_4$, (b) Li/LCE-H5/$LiFePO_4$, (c) Li/LCE-P4/$LiFePO_4$, and (d) Li/LCE-P5/$LiFePO_4$ cells.

$\pm$ 0.3 V and 3.1 $\pm$ 0.3 V for oxidation and reduction, respectively, indicating stable lithium-ion insertion and extraction (see Fig. 8). Although the curves vary, no distinct difference is evident between the planar and homeotropic electrolytes (see Table S4 for detailed calculation of average overpotential). The batteries were cycled five times at a scan rate of 5 mV s^{-1}. Minor peak shifts during the first and later cycles are likely due to side reactions forming a solid electrolyte interphase (SEI) layer, possibly involving trace impurities. Cycles 2–5 overlap with each other, except for minor shifts in current, but the voltage peak locations remain consistent, indicating good oxidation and reduction stability of the LCE-Xn (n = 4, 5) electrolytes.

Linear sweep voltammetry (LSV) was performed (1-time measurement per half cells), on Li/LCE-Xn (n = 1–5) half-cells at 22.4 °C to evaluate the onset oxidation potentials of the electrolytes. They are determined from the intersection of tangents drawn to the non-faradaic (background) region where the current is minimal, and the faradaic (reaction) region, where the current increases significantly. This value was found to be approximately 4.8 V as highlighted in the 4.5–5.0 V region in Fig. 9(a) for planar and Fig. 9(b) for homeotropic alignment.

3.4. Li/LCE/$LiPO_4$ battery performance

Since LCE-X1 and LCE-X2 showed <0.01 mS cm^{-1} ionic conductivity only batteries with LCE-Xn ($n \geq 3$) were subjected to charge–discharge cycling at varying current densities at room temperature. Cycling tests were conducted at various C-rates (C-rate is a measure of the rate at which a battery is charged or

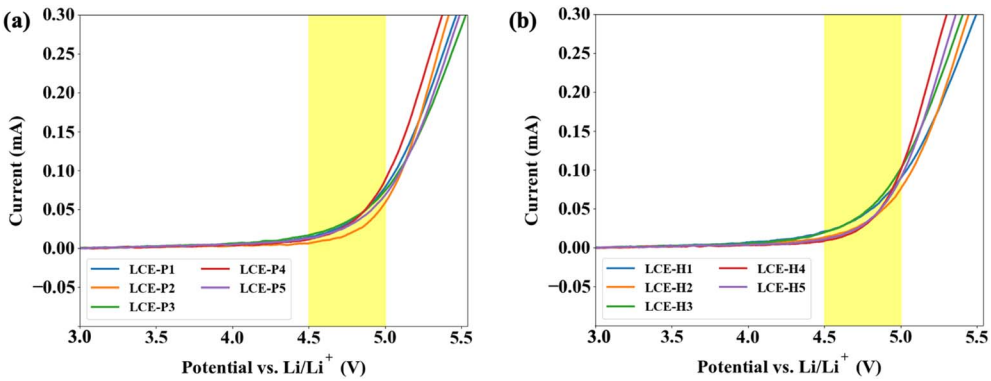

Fig. 9 Linear Sweep Voltammetry (LSV) of Li/LCE-Xn (n = 1, 2, 3, 4, 5) half cells showing the determination of the onset oxidation potential highlighted in the 4.5–5.0 V range and found to be ~4.8 V for (a) planar, and (b) homeotropic alignments.

discharged relative to its maximum capacity) to assess the durability of the different LCE systems (see Fig. 10).

For LCE-P5, P4, and P3 the initial discharge capacities at 0.1C were 132.9, 108.4, and 86.6 mAh g^{-1}, respectively. In homeotropic alignment, the order was the same with slightly higher values: 139.0, 125.9, and 95.3 mAh g^{-1}. Due to their largest (~1 mS cm^{-1}) ionic conductivity LCE-X5 (see Fig. 10(e and f)) exhibited the highest specific capacity with slightly higher values in the homeotropic cell. A notable divergence was observed in LCE-X3 (see Fig. 10(a and b)) and LCE-X4 (see Fig. 10(c and d)), where the planar-aligned sample showed significantly lower specific capacities. This agrees with the alignment-dependent differences in ionic conductivity, which were discussed in 3.2.

Fig. 11(a and c) shows the long-term stability results at room temperature at 0.1C. LCE-X4 demonstrated the most outstanding stability, retaining over 96% and 93% of its initial capacity after 300 cycles for planar and homeotropic alignments, respectively. LCE-X5 exhibited moderate (93% and 89%) retention, while LCE-X3 showed the most decline in performance, retaining only 84% and 83% for planar and homeotropic alignments, respectively. This underperformance can be attributed to its lower lithium-ion transference number and lower ionic conductivity, which likely accelerated degradation mechanisms.

Fig. 11(b and d) show the initial charge–discharge stability at increasing current densities. Higher C-rate results in a lower specific capacity. Conversely, a larger ionic content leads to higher overall initial and long-term discharge capacities. The fact that LCE-X5 which initially provided superior capacity, retained slightly less capacity over extended cycling compared to LCE-X4, may be attributed to high IL concentration in LCE-X5, which disrupts the alignment. Furthermore, rate capability analysis revealed that among all tested electrolytes,

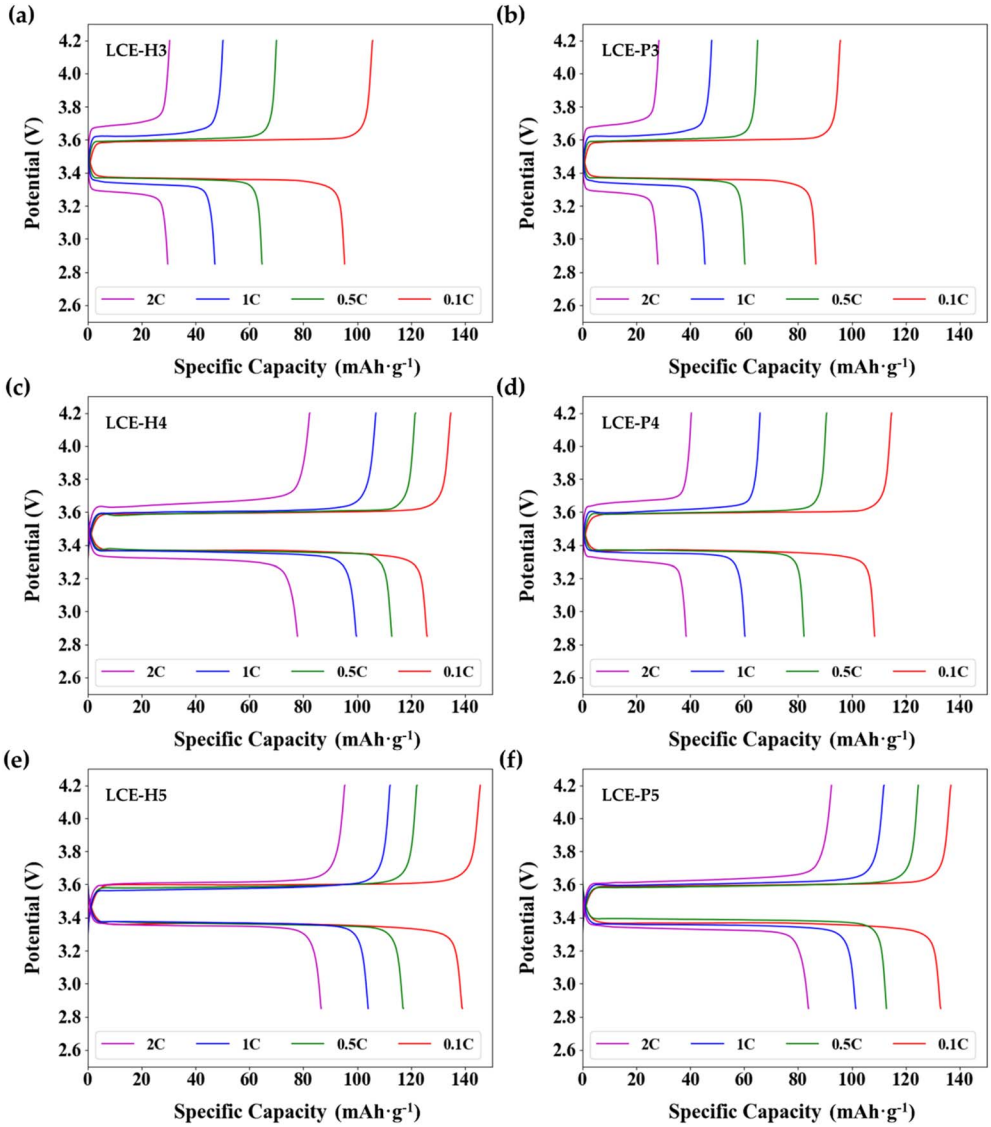

Fig. 10 Selected charge–discharge curves at room temperature (22.4 °C) during cycling at 0.1, 0.5, 1 and 2 C-rates: (a) LCE-H3, (b) LCE-P3, (c) LCE-H4, (d) LCE-P4, (e) LCE-H5, (f) LCE-P5.

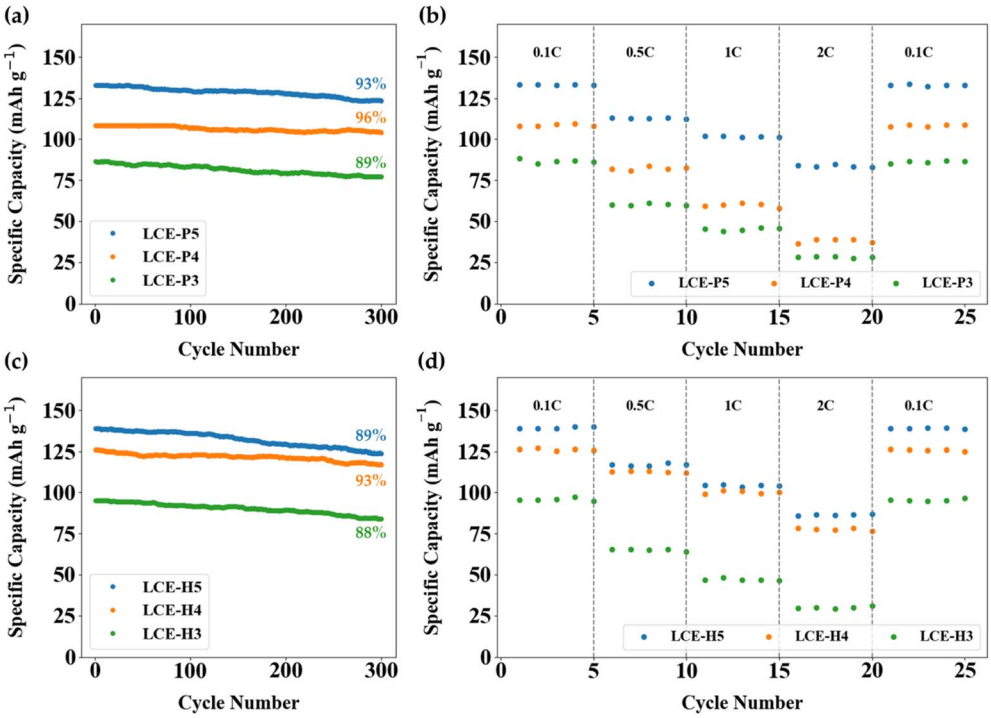

Fig. 11 Specific discharge capacity of Li/LCE-X*n*/LiFePO$_4$ (*n* = 3, 4, 5) during 300 cycles at 0.1C and room temperature: (a) planar alignment, (c) homeotropic alignment Rate performance of Li/LCE-X*n*/LiFePO$_4$ (*n* = 3, 4, 5) batteries at various C-rates at room temperature: (b) planar alignment, (d) homeotropic alignment.

batteries using LCE-X4 and LCE-X5 exhibited the best initial rate performance. Notably, most LCE-based batteries were able to recover nearly all their original capacity when the current density was returned to 0.1C. This indicates that the LCE-X*n* materials maintained structural and electrochemical integrity even under high-rate stress.

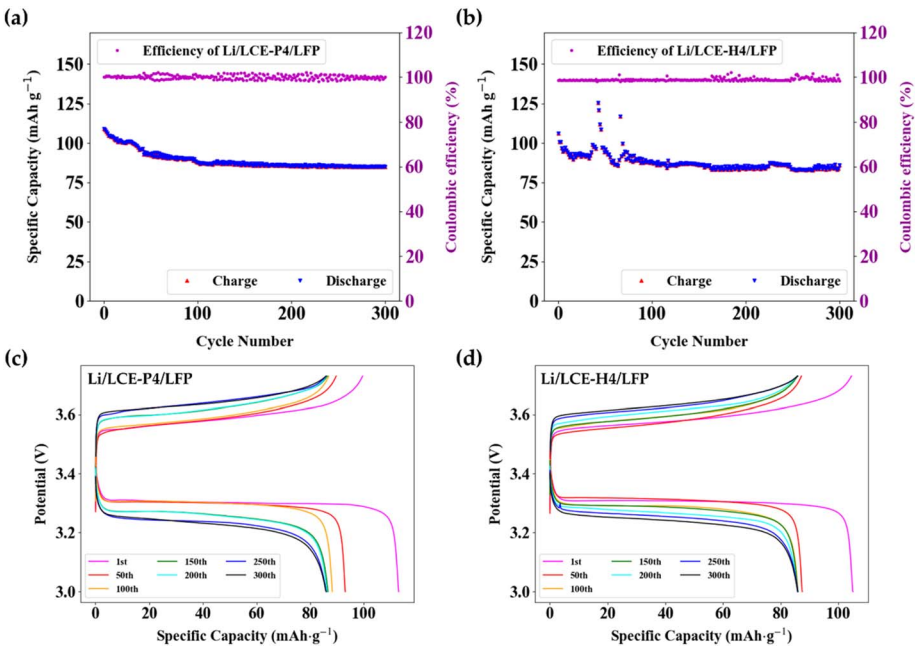

Fig. 12 Cycling performance of Li/LCE-X4/LiFePO$_4$ cells at 1C at room temperature. Cycle number dependence of specific capacity (left axis) and coulombic efficiency (right axis) for planar (a) and homeotropic alignment (b). Potential *versus* specific capacity (charge–discharge profiles) for planar (c) and homeotropic (d) alignment.

Fig. 12 shows the battery long-term performance under 1C charge–discharge cycles. Lithium metal batteries assembled with a Li/LCE-X4/$LiFePO_4$ configuration retained over 78% and 81% of their initial capacity after 300 cycles, with a coulombic efficiency ~99% for planar and homeotropic electrolytes, respectively (see Fig. 12(a and b)). Although a gradual decline in specific capacity was observed during prolonged cycling, the cell structure remained mechanically intact as seen in Fig. 12(c and d).

3.5. Post-cycle analysis

Cycled electrolytes were extracted in an Ar-gas filled glovebox by cutting open the CR2032 coin cell casings along their circumference. Post-cycling, the electrolytes were observed to bond firmly to the LFP cathode material while detaching cleanly from the anode. SEM images were taken of the LCE-H4 and LCE-P5 bulk (Fig. 13(a and b)). A 45° tilted cross-section of LCE-P5 (Fig. 13(c)) was also imaged, showing both the electrolyte surface from the anode side and the LFP attached to the bulk. The bulk cross-sections reveal a porous structure containing small particles; however, the overall elastomer morphology remains consistent and shows minimal degradation, indicating good contact was maintained at the cathode surface.

As the capability to perform SEM analysis in a controlled dry air or Ar-filled environment was not available, the lithium metal anodes were transferred to the SEM facility inside a vacuum desiccator to minimize oxidation during transport. Using plastic tweezers, the anode was quickly moved from the desiccator to the SEM sample holder, allowing minimal air exposure before the chamber was evacuated. Although a small amount of oxidation was unavoidable during this transfer, the SEM analysis (Fig. 14) successfully revealed a dense morphology devoid of dendritic protrusions for anodes cycled with both LCE-X4 and LCE-X5 electrolytes. Among these, LCE-X4 appears to possess superior interfacial compatibility with metallic lithium,

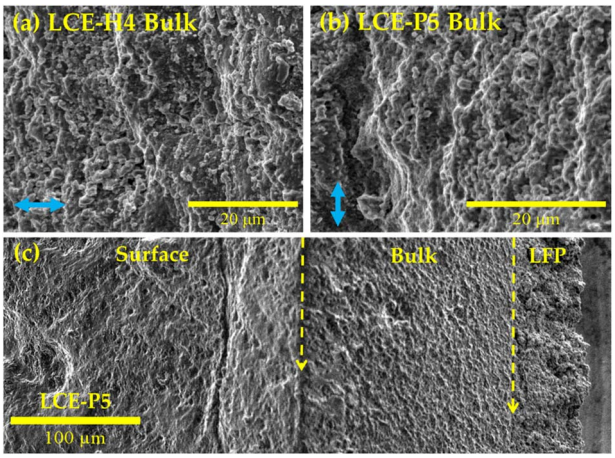

Fig. 13 SEM images of electrolytes after 300 charge–discharge cycles showing cross-sectional views of the bulk material for (a) LCE-H4; (b) LCE-P5; and (c) 45° tilt angle view of LCE-P5 electrolyte anode-side surface, bulk and LFP cathode. Blue arrows indicate the nematic director of the elastomer.

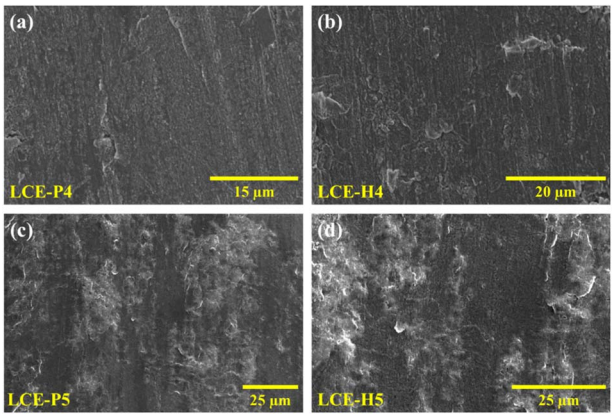

Fig. 14 SEM images of lithium metal anode surfaces after 300 charge–discharge cycles in contact with different electrolytes: (a) LCE-P4, (b) LCE-H4, (c) LCE-P5, and (d) LCE-H5.

effectively inhibiting lithium nucleation and growth, which suggests it can sustain long-term cycling as can be seen from the smooth structure of the corresponding anode surfaces shown in Fig. 14(a and b). The anodes cycled with LCE-X5, shown in Fig. 14(c and d), also looks similar with no visible cracks, but it appears slightly more oxidized, which could be an artifact of the SEM handling process.

We also tested the polarizing microscopy (POM) textures of LCE-H4 and LCE-P5 samples after 300 cycles. For that they were first vacuum-dried, then cooled to −70 °C using liquid nitrogen and fractured along the center of the circular LCE electrolyte discs. POM images shown in Fig. S13 reveal that, although Li-ion migration and the accumulation of $LiFePO_4$ at the interface during cycling caused the images to appear darker, the molecular alignment remains largely unchanged as also evidences by the X-ray diffraction patterns.

2D Wide Angle X-ray (WAXS) profiles of LCE-Xn (n = 3–5) after 300 charge–discharge cycles are shown in Fig. 15 after 5 minutes exposure time. The top row (planar) in Fig. 15(a–c) and bottom row (homeotropic) in Fig. 15(c and d) shows the profiles with the original director alignment more-or-less vertical direction.

Preparation of samples LCE-Xn (n = 3–5) for XRD analysis differed based on the sample's alignment. The elastomer's thickness did not change post-cycling, remaining at ~100 μm. For planar samples intended for WAXS, the cathode was separated using a microtome to cut a 10 μm layer into the elastomer from the cathode side. This resulted in a 90 μm thick circular sample, which was used without drying to mimic the initial WAXS measurement conditions. For the homeotropic samples intended for WAXS, the cathode was separated in a similar manner; however, a 90 μm thick cross-section was then cut perpendicular to the elastomer's circular plane. This process yielded a thin rectangular sheet (90 μm × 90 μm × 1 cm) that was used for WAXS analysis.

In comparing with Fig. S2 and S3 of the SI we conclude that the alignments remain basically the same post cycle as the original one (degree of alignment best in LCE-X3 with S ~0.26 ±

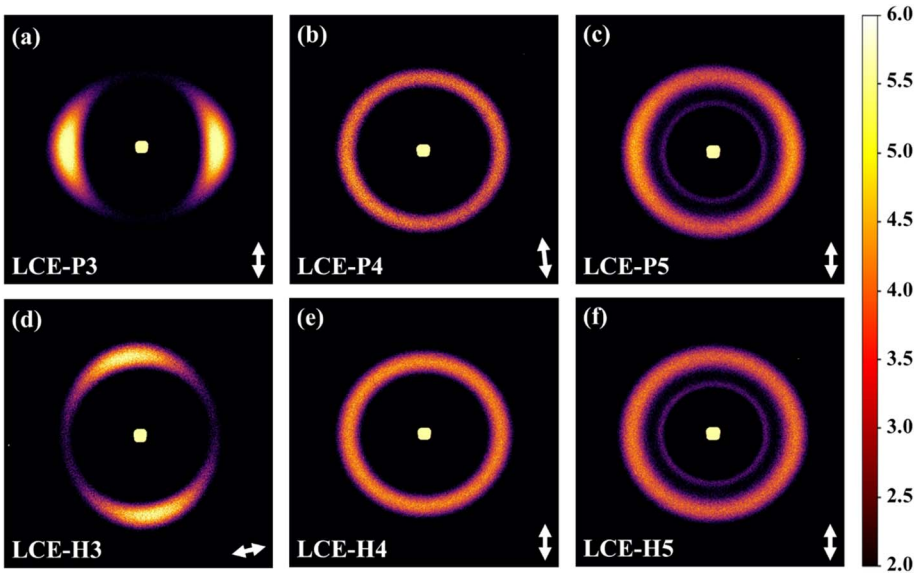

Fig. 15 2D Wide Angle X-ray (WAXS) profiles of LCE-Xn (n = 3–5) after 300 charge–discharge cycles. (a), (b) and (c) show results for LCP-P3,4 and 5, and (d), (e) and (f) show 2D profiles for LCP-H3,4 and 5, respectively. White double-sided arrows indicate the original alignment directions. Exposure time is 5 minutes for all samples.

Table 1 Comparative benchmarking of key electrochemical properties for different polymer electrolyte systems at room temperature

Electrolytes	Ionic conductivity (RT, S cm^{-1})	Li^+ transference number	Electrochemical window (V *vs.* Li/Li^+)	References
PEO based (SPE)	10^{-8}–10^{-5}	~0.1–0.3	~3.8–4.2	13, 14 and 21
PVDF-HFP based (GPE)	10^{-4}–10^{-3}	~0.2–0.4	~4.3–5.2	54 and 55
Single-ion network (SICNP)	~1.1×10^{-3}	~0.94	~4.5–4.8	56
Polysiloxane-based (SIPE)	~7×10^{-4}	~0.53–0.89	~4.8–5.2	57 and 58
LCE-X4	~1×10^{-4}	~0.65–0.67	~4.8	[This work]
LCE-X5	~1×10^{-3}	~0.69–0.71	~4.8	[This work]

0.01 and getting worse in LCE-X4 with S ~0.17 ± 0.06 and LCE-X5 with S ~0.14 ± 0.02). The only difference if the appearance of a second ring at $q \sim 0.8$ Å^{-1} for the LCE-X5 samples, shown in Fig. S14. Tentatively we attribute this to separated IL component after 300 cycles at this high 66.7 wt% IL concentration.

4. Conclusions

In this study, we systematically investigated the effect of macroscopic director alignment on the electrochemical performance of IL infused LCE electrolytes, presenting the first comparison between planar and homeotropic alignment configurations in an LCE-based lithium-ion battery.

A primary objective was to find out which alignment performs better. Our findings reveal a non-linear relationship that is critically dependent on IL concentration. At low IL content (LCE-X1, X2), the planar alignment exhibited slightly higher ionic conductivity, which we attributed to the formation of smectic-like domains that favor ion transport parallel to the electrodes. However, a distinct crossover occurred at moderate IL loadings (LCE-X3, X4). In this optimal range, the homeotropic alignment was demonstrably superior, achieving 2–3 times higher ionic conductivity, a lower activation energy, and a higher Li-ion transference number. This translated directly to improved full-cell performance, where homeotropic samples delivered higher initial specific capacities. Finally, at the highest IL content (LCE-X5), the IL disrupts the LCE's molecular order, causing the system to behave somewhat isotropic, and the performance of both planar and homeotropic samples nearly converged.

By tuning the IL content and alignment, we achieved a quasi-solid (gel-polymer) electrolyte system with up to ~1 mS cm^{-1} ionic conductivity for LCE-X5 and a high Li-ion transference number in the 0.62–0.69 range, which is significantly higher than conventional PEO-based electrolytes. The LCE-X4 samples demonstrated the best overall balance of properties, with the Li/LCE-X4/LFP full cells delivering stable cycling for over 300 cycles at 1C, maintaining over 80% capacity retention. Furthermore, symmetric Li/LCE-Xn/Li cells ($n \geq 2$) exhibited excellent lithium plating/stripping stability for over 300 hours, confirming the LCE matrix is effective at suppressing dendrite growth.

This study provides a foundational comparison of planar and homeotropic alignments, but further work is needed to optimize the system. While we demonstrate a clear proof-of-

concept, the mechanical properties of the electrolytes at high IL loadings were not quantitatively benchmarked. Furthermore, this work focused on a nematic-phase LCE.

In Table 1 we compare the key electrochemical properties of LCE-X4 and LCE-X5 with different polymer electrolyte systems at room temperature. Our system's electrochemical stability window of ~4.8 V is comparable to the other benchmark systems. Crucially, both our LCE-X4 and LCE-X5 systems demonstrate exceptionally high Li^+ transference numbers t_{Li^+} ranging from approximately 0.65 to 0.71. This range is more than double that of typical PEO or the top-tier gel polymer electrolytes PVDF-HFP systems. This shows that LCE-X4 materials offer a more efficient pathway for lithium-ion transport. Notably, higher t_{Li^+} values help reduce concentration polarization and suppress dendrite formation, thereby enhancing the interfacial stability and compatibility between the electrolyte and electrode. This, in turn, leads to improved coulombic efficiency and overall battery performance.

On the other hand, the transference number of our system is still lower than those of true single-ion conductors – like the SICNP or Polysiloxane-based Single-Ion Polymer Electrolyte (SIPE) systems, which are designed to immobilize anions. This indicates that to further enhance the ionic conductivity and the transference number of our LCE based electrolytes, a particularly promising route is the synthesis of single ion conducting LCEs, where the anion is grafted onto the polymer backbone. Such a system could theoretically combine the high Li^+ transference numbers seen in SIPEs with the directional transport channels of an aligned liquid crystal, representing a significant step toward an ideal solid-state electrolyte.

Future perspectives should focus on enhancing the anisotropic effect. This could be achieved by designing LCE systems with stronger, more stable smectic ordering that can be maintained even at high IL concentrations. Finally, a deeper mechanistic study is required to fully decouple the factors contributing to dendrite suppression, including the relative contributions of mechanical stiffness and uniform ion flux.

In summary, this work establishes LCE alignment as a critical and tunable design parameter for optimizing ion transport. Our findings demonstrate that an aligned LCE host is a highly effective strategy for developing high-performance, quasi-solid (gel-polymer) electrolytes that successfully balance high ionic conductivity with an excellent lithium-ion transference number.

5. Experimental techniques

5.1. Material characterization

Polarized Optical Microscopy (POM) was conducted using an Olympus BX60 polarizing microscope equipped with a Polaviz thermal stage, allowing precise temperature control at a rate of 0.1 °C min^{-1} during both heating and cooling cycles.

Scanning Electron Microscopy (SEM) was performed with a Quanta 450 FEG instrument to examine the microstructure of the electrolyte films. Prior to imaging, samples were sputter-coated with a thin layer of gold for 30 seconds to enhance conductivity.

Fourier Transform Infrared (FTIR) spectroscopy was used to verify the crosslinking of the liquid crystal elastomer (LCE) network. Measurements were conducted using a Bruker FTIR spectrometer in transmission mode. Precursor solutions were deposited onto a KBr crystal, and spectra were collected both before and after UV polymerization. Each spectrum represented an average of 64 scans with a resolution of 2 cm^{-1} over a spectral range of 400 to 4000 cm^{-1}. Wide-angle X-ray scattering (WAXS) was employed to determine the nematic order parameter of the electrolyte films. Measurements were carried out on a Xeuss 3.0 system equipped with a Cu X-ray source at 22.4 °C. The experimental setup included a detector distance of 55 mm, an exposure time of 300 s, and a chamber pressure of 0.1 mbar, with the sample temperature maintained at 22.3 °C.

5.2. Electrochemical characterization

All cell assembly procedures were conducted in a Purelab-HE-2GB argon-filled glove box, with oxygen and moisture levels maintained below 0.1 ppm. Electrochemical performance was evaluated using CR2032-type coin cells. To assess ionic conductivity, a custom-designed symmetric Stainless Steel (SS)/LCE-SPE/SS cells with precise 1 mm × 1 mm surface area and 0.1 mm thickness were constructed and evaluated using an Autolab PGSTAT302N electrochemical workstation. Electrochemical impedance spectroscopy was employed to determine the ionic resistance of the solid polymer electrolyte over a temperature range of 20 °C to 80 °C. Impedance measurements were conducted over a frequency range of 0.1 Hz to 10^6 Hz with an applied AC voltage amplitude of 50 mV.

The electrochemical stability window of the LCE-based polymer electrolyte (LCE-X*n*) was evaluated using linear sweep voltammetry in Li/LCE-X*n* cells. The voltage was scanned from 2 V to 5 V at a rate of 0.1 mV s^{-1}. To assess redox stability, cyclic voltammetry was performed on Li/LCE-X*n*/$LiFePO_4$ cells under the same scan rate, with a voltage range of 2 V to 4.5 V.

5.3. LCE-X*n* battery assembly

For coin cell assembly, the LCE-X*n* samples (where X = P for planar or H for homeotropic alignment, and n = 1, 2, 3, 4, 5 corresponding to 0.05, 0.25, 0.5, 1.0, and 1.5 g of infused ionic liquid, respectively) were placed between a $LiFePO_4$ (LFP) cathode disc and a lithium metal anode. The lithium metal anodes were chemically polished inside an Ar-filled glovebox (PureLab HE) prior to assembly.[59]

Galvanostatic charge–discharge tests and rate capability measurements were performed using a multichannel NEWARE Battery Testing System (5 V, 10 mA), operating within a voltage window of 2.0–5.0 V. The cycling performance of the Li/LFP cells was evaluated at various C-rates to investigate long-term electrochemical stability and capacity retention.

Author contributions

Conceptualization, A. J. and W. X.; methodology, A. J. and W. X.; software, Z. S.; validation, Z. S., A. J. and W. X.; formal analysis, Z. S. and A. J; investigation, Z. S.; resources, A. J. and W. X.; data

curation, Z. S.; writing—original draft preparation, Z. S. and A. J; writing—review and editing, W. X.; visualization, Z. S.; supervision, A. J.; All authors have read and agreed to the published version of the manuscript.

Conflicts of interest

The authors declare no conflicts of interest.

Data availability

The data supporting this article have been included as part of the supplementary information (SI). Supplementary information: the materials compositions, FTIR spectra, 2dWAXS profiles, additional POM and FE-SEM images, Nyquist plots of electrochemical impedance spctroscopy and additional post cyccle POM and WAXS results. See DOI: https://doi.org/10.1039/d5ra07527k.

Acknowledgements

We acknowledge useful discussions with Prof. Then Kyu at The University of Akron.

References

1 M. Li, J. Lu, Z. Chen and K. Amine, *Adv. Mater.*, 2018, **30**, 1800561.
2 J. B. Goodenough and K. S. Park, *J. Am. Chem. Soc.*, 2013, **135**, 1167–1176.
3 H. Zhou, R. Zhao, Y. Xiao, L. Feng, Y. Yang, L. Bao and J. Wang, *J. Polym. Sci.*, 2020, **58**, 3480–3487.
4 M. Park, X. Zhang, M. Chung, G. B. Less and A. M. Sastry, *J. Power Sources*, 2010, **195**, 7904–7929.
5 K. S. Ngai, S. Ramesh, K. Ramesh and J. C. Juan, *Ionics*, 2016, **22**, 1259–1279.
6 V. Etacheri, R. Marom, R. Elazari, G. Salitra and D. Aurbach, *Energy Environ. Sci.*, 2011, **4**, 3243–3262.
7 N. Kamaya, K. Homma, Y. Yamakawa, M. Hirayama, R. Kanno, M. Yonemura, T. Kamiyama, Y. Kato, S. Hama, K. Kawamoto and A. Mitsui, *Nat. Mater.*, 2011, **10**, 682–686.
8 B. Scrosati, J. Hassoun and Y. K. Sun, *Energy Environ. Sci.*, 2011, **4**, 3287–3295.
9 H. Lee, R. Li, C. R. Piedrahita, J. Cao and T. Kyu, *J. Energy Storage*, 2023, **64**, 107138.
10 H. Lee, J. Jeong, J. Parrondo, S. Zamani, D. Atienza and T. Kyu, *ACS Appl. Mater. Interfaces*, 2023, **15**, 27173–27182.
11 D. Bresser, S. Lyonnard, C. Iojoiu, L. Picard and S. Passerini, *Mol. Syst. Des. Eng.*, 2019, **4**, 779–792.
12 R. Onozuka, C. Piedrahita, Y. Yanagida, K. Adachi, Y. Tsukahara and T. Kyu, *Solid State Ionics*, 2020, **346**, 115182.
13 Z. Xue, D. He and X. Xie, *J. Mater. Chem. A*, 2015, **3**, 19218–19253.
14 T. N. T. Phan, S. Issa and D. Gigmes, *Polym. Int.*, 2019, **68**, 7–13.
15 C. Piedrahita, V. Kusuma, H. B. Nulwala and T. Kyu, *Solid State Ionics*, 2018, **322**, 61–68.
16 M. Echeverri, N. Kim and T. Kyu, *Macromolecules*, 2012, **45**, 6068–6077.
17 K. Kobayashi, G. Pagot, K. Vezzù, F. Bertasi, V. Di Noto and Y. Tominaga, *Polym. J.*, 2021, **53**, 149–155.
18 L. Seidl, R. Grissa, L. Zhang, S. Trabesinger and C. Battaglia, *Adv. Mater. Interfaces*, 2022, **9**, 2100704.
19 C. Feng and T. Kyu, *Electrochim. Acta*, 2020, **330**, 135320.
20 W. S. Young and T. H. Epps, *Macromolecules*, 2012, **45**, 4689–4697.
21 M. Armand and J. M. Tarascon, *Nature*, 2008, **451**, 652–657.
22 I. J. Kim, K. S. Kim and J. H. Lee, *Appl. Chem. Eng.*, 2020, **31**, 305–309.
23 T. Onuma, E. Hosono, M. Takenouchi, J. Sakuda, S. Kajiyama, M. Yoshio and T. Kato, *ACS Omega*, 2018, **3**, 159–166.
24 P. S. Drzaic, *Liquid Crystal Dispersions*, World Scientific, River Edge, NJ, 1995, p. 448.
25 A. Yoshizawa, *Polym. J.*, 2012, **44**, 490–502.
26 R. Rondla, J. C. Y. Lin, C. T. Yang and I. J. B. Lin, *Langmuir*, 2013, **29**, 11779–11785.
27 Z. Zhang, Z. You and D. Chu, *Light: Sci. Appl.*, 2014, **3**, e213.
28 M. Warner and E. Terentjev, *Liquid Crystal Elastomers*, 2003, vol. 120.
29 H. Finkelmann, *Angew Chem. Int. Ed. Engl.*, 1987, **26**, 816–824.
30 T. Kato, *Science*, 2002, **295**, 2414–2418.
31 C. Feng, C. P. H. Rajapaksha, J. M. Cedillo, C. Piedrahita, J. Cao, V. Kaphle, B. Lüssem, T. Kyu and A. Jákli, *Macromol. Rapid Commun.*, 2019, **40**, 1900299.
32 X. Wang, Z. He, R. Yan, H. Niu, W. He and Z. Miao, *Chem. Eng. J.*, 2025, **503**, 158552.
33 Z. Siddiquee, H. Lee, W. Xu, T. Kyu and A. Jákli, *Batteries*, 2025, **11**, 106.
34 Y. Wang, C. J. Zanelotti, X. Wang, R. Kerr, L. Jin, W. H. Kan, T. J. Dingemans, M. Forsyth and L. A. Madsen, *Nat. Mater.*, 2021, **20**, 1255–1263.
35 T. Ohtake, M. Ogasawara, K. Ito-Akita, N. Nishina, S. Ujiie, H. Ohno and T. Kato, *Chem. Mater.*, 2000, **12**, 782–789.
36 J. Anthony Dicks and C. Woolard, *Macromol. Mater. Eng.*, 2025, **310**, 2400445.
37 M. O. Saed, A. H. Torbati, D. P. Nair and C. M. Yakacki, *J. Visualized Exp.*, 2016, **2016**, e53546.
38 M. Zhang, H. Shahsavan, Y. Guo, A. Pena-Francesch, Y. Zhang and M. Sitti, *Adv. Mater.*, 2021, **33**, 2008605.
39 J. Anthony Dicks and C. Woolard, *Macromol. Mater. Eng.*, 2025, **310**, 2400445.
40 S. B. Aziz and Z. H. Z. Abidin, *J. Soft Matter.*, 2013, **2013**, 323868.
41 P. H. Hermans and P. Platzek, *Kolloid-Z.*, 1939, **88**, 68–72.
42 R. S. Stein, *J. Polym. Sci.*, 1958, **31**, 327–334.
43 R. J. Samuels, *X-ray diffraction methods in polymer science*, 1970, vol. 6.
44 M. K. Kang, E. J. Cha, H. H. Song and Y. H. Na, *Heliyon*, 2019, **5**, e02421.
45 J. V. Selinger, *Introduction to the Theory of Soft Matter*, 2016.

46 A. Ciferri, *Polymer Liquid Crystals*, Elsevier, 1st edn., 1982.
47 Q. Lin, D. Kundu, M. Skyllas-Kazacos, J. Lu, D. Zhao, K. Amine, L. Dai and D.-W. Wang, *Adv. Mater.*, 2024, **36**, 2406151.
48 J. Wan, Y. Hao, Y. Shi, Y. X. Song, H. J. Yan, J. Zheng, R. Wen and L. J. Wan, *Nat. Commun.*, 2019, **10**, 3265.
49 Q. Ruan, M. Yao, D. Yuan, H. Dong, J. Liu, X. Yuan, W. Fang, G. Zhao and H. Zhang, *Nano Energy*, 2023, **106**, 108087.
50 F. Chen, X. Wang, M. Armand and M. Forsyth, *Nat. Mater.*, 2022, **21**, 1175–1182.
51 X. Chen, W. Liao, D. Chen, Y. Huang and C. Liu, *Compos. Sci. Technol.*, 2024, **245**, 110327.
52 P. G. Bruce, J. Evans and C. A. Vincent, *Solid State Ionics*, 1988, **28–30**, 918–922.
53 J. Evans, C. A. Vincent and P. G. Bruce, *Polymer*, 1987, **28**, 2324–2328.
54 J. Jie, Y. Liu, L. Cong, B. Zhang, W. Lu, X. Zhang, J. Liu, H. Xie and L. Sun, *J. Energy Chem.*, 2020, **49**, 80–88.
55 G. Chen, F. Zhang, Z. Zhou, J. Li and Y. Tang, *Adv. Energy Mater.*, 2018, **8**, 1801219.
56 X. Xu, J. Chen, J. Li, J. Shen, P. Lin, Z. Wang, Z. Guo, J. Sun, B. Huang and T. Zhao, *J. Am. Chem. Soc.*, 2025, **147**, 25896–25909.
57 C. Fu, M. Iacob, Y. Sheima, C. Battaglia, L. Duchêne, L. Seidl, D. M. Opris and A. Remhof, *J. Mater. Chem. A*, 2021, **9**, 11794–11801.
58 R. Rohan, K. Pareek, Z. Chen, W. Cai, Y. Zhang, G. Xu, Z. Gao and H. Cheng, *J. Mater. Chem. A*, 2015, **3**, 20267–20276.
59 W. Tang, X. Yin, Z. Chen, W. Fu, K. P. Loh and G. W. Zheng, *Energy Storage Mater.*, 2018, **14**, 289–296.